
Preclinical Kinetic Analysis of the Caspase-3/7 PET Tracer ^{18}F -C-SNAT: Quantifying the Changes in Blood Flow and Tumor Retention After Chemotherapy

Mikael Palner¹, Bin Shen¹, Jongho Jeon¹, Jianguo Lin^{1,2}, Frederick T. Chin¹, and Jianghong Rao¹

¹Department of Radiology, Molecular Imaging Program at Stanford, Stanford University School of Medicine, Stanford, California; and ²Key Laboratory of Nuclear Medicine, Jiangsu Institute of Nuclear Medicine, Wuxi, China

Early detection of tumor response to therapy is crucial to the timely identification of the most efficacious treatments. We recently developed a novel apoptosis imaging tracer, ^{18}F -C-SNAT (C-SNAT is caspase-sensitive nanoaggregation tracer), that undergoes an intramolecular cyclization reaction after cleavage by caspase-3/7, a biomarker of apoptosis. This caspase-3/7-dependent reaction leads to an enhanced accumulation and retention of ^{18}F activity in apoptotic tumors. This study aimed to fully examine *in vivo* pharmacokinetics of the tracer through PET imaging and kinetic modeling in a preclinical mouse model of tumor response to systemic anticancer chemotherapy. **Methods:** Tumor-bearing nude mice were treated 3 times with intravenous injections of doxorubicin before undergoing a 120-min dynamic ^{18}F -C-SNAT PET/CT scan. Time-activity curves were extracted from the tumor and selected organs. A 2-tissue-compartment model was fitted to the time-activity curves from tumor and muscle, using the left ventricle of the heart as input function, and the pharmacokinetic rate constants were calculated. **Results:** Both tumor uptake (percentage injected dose per gram) and the tumor-to-muscle activity ratio were significantly higher in the treated mice than untreated mice. Pharmacokinetic rate constants calculated by the 2-tissue-compartment model showed a significant increase in delivery and accumulation of the tracer after the systemic chemotherapeutic treatment. Delivery of ^{18}F -C-SNAT to the tumor tissue, quantified as K_1 , increased from $0.31 \text{ g}(\text{mL}\cdot\text{min})^{-1}$ in untreated mice to $1.03 \text{ g}(\text{mL}\cdot\text{min})^{-1}$ in treated mice, a measurement closely related to changes in blood flow. Accumulation of ^{18}F -C-SNAT, quantified as k_3 , increased from 0.03 to 0.12 min^{-1} , proving a higher retention of ^{18}F -C-SNAT in treated tumors independent from changes in blood flow. An increase in delivery was also found in the muscular tissue of treated mice without increasing accumulation. **Conclusion:** ^{18}F -C-SNAT has significantly increased tumor uptake and significantly increased tumor-to-muscle ratio in a preclinical mouse model of tumor therapy. Furthermore, our kinetic modeling of ^{18}F -C-SNAT shows that chemotherapeutic treatment increased accumulation (k_3) in the treated tumors, independent of increased delivery (K_1).

Key Words: tumor therapy response; apoptosis; caspase-3/7; systemic chemotherapy; preclinical PET

J Nucl Med 2015; 56:1415–1421

DOI: 10.2967/jnumed.115.155259

Early detection of tumor response to therapy is crucial to shorten the period of uncertainty after starting treatment and to quickly identify the most effective treatment of individual cancer patients. Tumors are highly heterogeneous and can respond differently to the same treatments (1); a successful treatment therefore requires a more personalized medicine approach tailored to individual tumor biology. To realize this vision, oncologists need a tool to quickly assess tumor response to the selected treatment (2).

Current clinical methods to assess treatment response are based on size measurements of tumors using CT or MR imaging under the guidelines of the Response Evaluation Criteria in Solid Tumors (3). In addition, PET imaging of ^{18}F -FDG metabolism in tumors (4,5) can provide a functional measurement as described by the PET Response Criteria in Solid Tumors (6). Response Evaluation Criteria in Solid Tumors-based size measurement lacks sensitivity for early assessment of response, as it can take many weeks from treatment initiation to actual size changes that can be detected. Furthermore, tumor size shrinkage may not occur in the case of cytostatic and molecularly targeted therapy even when the treatment is effective (7). PET Response Criteria in Solid Tumors is based on a decrease in the ^{18}F -FDG metabolism in response to fewer living tumor cells; however, a decrease in signal is unfavorable and limits detection in tumors, which are less metabolically active. Furthermore, ^{18}F -FDG uptake is not limited to tumor cells and may be biased by higher metabolism in nearby inflammatory (8) or hypoxic tissues (9–11) that are also affected by the treatment, especially radiotherapy. It has been advised that radiologists wait a minimum of 10 d after therapy before performing ^{18}F -FDG PET to bypass these flare effects (6).

Many anticancer treatments such as chemotherapy and radiotherapy induce tumor cell death by initiating biologic pathways, such as apoptosis (12). Apoptosis is characterized by the activation of a series of proteases, starting with the release of cytochrome c. This release leads to self-assembly of the apoptotic protease-activating factor 1 and caspase-9 into the apoptosome, which in turn activates caspase-3/7 and ultimately initiates cell death by increasing DNA cleavage (12). Simultaneously, blebbing of the cell wall in the dying cells exposes phosphatidylserine or phosphatidylethanolamine to the cell surface (12). PET tracers targeting biomarkers in the apoptotic pathway could offer a means to monitor the degree of cell death after anticancer treatments and, in addition, to image other apoptosis-related physiologic processes or diseases such as ischemia or dementia (13,14).

Received Jan. 30, 2015; revision accepted Apr. 13, 2015.

For correspondence or reprints contact: Jianghong Rao, Molecular Imaging Program at Stanford, Department of Radiology, Stanford University School of Medicine, 1201 Welch Rd., Rm. P093, Stanford, CA 94305-5484.

E-mail: jrao@stanford.edu

Published online Jun. 4, 2015.

COPYRIGHT © 2015 by the Society of Nuclear Medicine and Molecular Imaging, Inc.

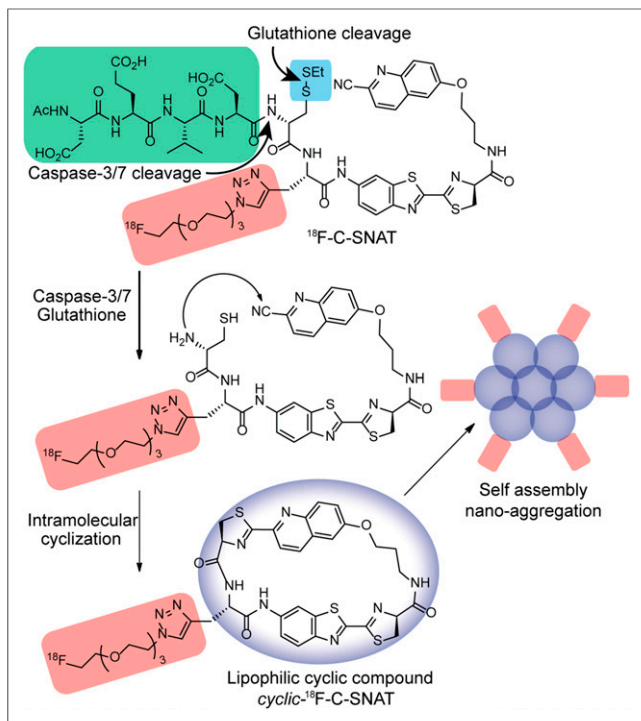


FIGURE 1. Design of ^{18}F -C-SNAT and proposed mechanism for imaging apoptosis. ^{18}F -C-SNAT is processed by caspase-3 cleavage of peptide DEVD-X (green) sequence and by glutathione reduction of disulfide bond (blue) to generate free cysteine and 2-cyano-6-hydroxyquinoline that undergo fast intramolecular cyclization forming *cyclic*- ^{18}F -C-SNAT. Increased lipophilicity of cyclized product leads to formation of *cyclic*- ^{18}F -C-SNAT lipophilic aggregates.

Several PET tracers targeting apoptosis biomarkers have been reported. ^{18}F -annexin-V (15) and ^{18}F -FPDyramycin (16) bind successfully to the extruded phosphatidylserine and phosphatidylethanolamine after membrane blebbing in vitro but showed a limited uptake in mouse models of tumor treatment response with a maximum approximately 1–2 percentage injected dose per gram (%ID/g) in treated tumors and a tumor-to-muscle ratio of approximately 1–3, depending on the tumor type. Another class of PET tracers is based on caspase-3 inhibitors, one of which, ^{18}F -(S)-1-((1-(2-fluoroethyl)-1H-[1,2,3]-triazol-4-yl)methyl)-5-(2(2,4-difluorophenoxy)methyl)pyrrolidine-1-sulfonyl)isatin (17), has undergone evaluation in healthy humans (18); however, the tumor uptake in chemotherapeutic-treated mice is also limited, with approximately 1 %ID/g maximum and significant treatment response reported only from a small subset of the tumor region (19). To generate better retention of the product in apoptotic cells, a novel class of tracers takes advantage of the cleavage activity of the effector enzyme caspase-3/7, including ^{18}F -CP-18 (20) and ^{18}F -C-SNAT (C-SNAT is caspase-sensitive nanoaggregation tracer) developed by us (21).

Caspase-3/7 cleaves a specific protein sequence DEVD-X (Asp-Glu-Val-Asp-X, X being any amino acid) to activate caspase-6. We have developed a novel method for imaging protease activity (Fig. 1), in which cleavage of the peptide substrate initializes an intramolecular cyclization reaction (22). The higher lipophilicity of the cyclic product leads to the formation of nanoaggregates and thus enhanced retention. This approach has been demonstrated for the detection of apoptosis of tumor xenografts treated with anticancer chemotherapeutics in a nude mouse with fluorescence imaging (23)

and MR imaging (24). A proof-of-principle study of the PET imaging of apoptosis of tumor cells that locally received chemotherapeutics (21) has recently been described with ^{18}F -C-SNAT. In the current work, we presented a quantitative in vivo kinetic analysis and evaluation of ^{18}F -C-SNAT for PET imaging of tumor apoptosis in a more clinically relevant chemotherapy cancer model.

All PET studies attempting to assess the tumor response to therapy have to examine the effect of increased blood flow after both chemotherapy (25,26) and radiotherapy (27). We have hitherto compared our active apoptosis PET tracer ^{18}F -C-SNAT with inactive control probe to account for this effect (21), but this is both time consuming and costly, especially for a human study. In this paper, we take a different approach to using full in vivo pharmacokinetic quantification of the tracer to account for the changes in blood flow. The effects of systemic chemotherapeutic treatment on blood flow and tumor retention of the tracer are assessed in mice, and an improved radiochemistry is presented. Our results show that ^{18}F -C-SNAT has a significantly increased tumor uptake and significantly increased tumor-to-muscle ratio in a preclinical mouse model of tumor therapy. Furthermore, our 2-compartment kinetic modeling of ^{18}F -C-SNAT shows that chemotherapeutic treatment increased accumulation (k_3) in the treated tumors, independent of increased delivery (K_1).

MATERIALS AND METHODS

General

Tris(2-benzimidazolylmethyl)amines (BimC₄A)₃, dimethylformamide, copper (II) sulfate (CuSO₄), and sodium ascorbate (NaAsc)

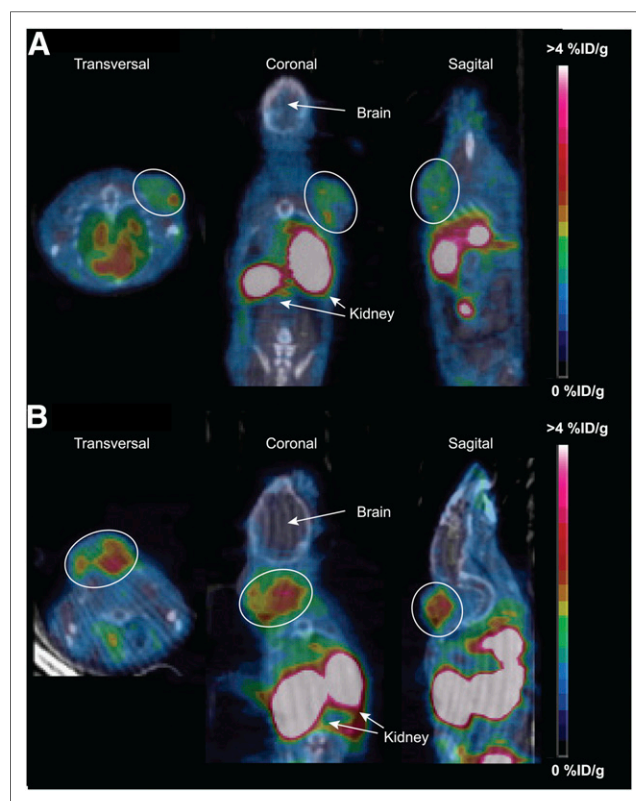


FIGURE 2. Representative coregistered ^{18}F -C-SNAT PET/CT images from 2 mice with xenografted HeLa tumors. (A) Untreated mouse. (B) Treated mouse. Summed images from 45 to 60 min and reconstructed using 3-dimensional ordered-subset expectation maximization. White circles mark tumors.

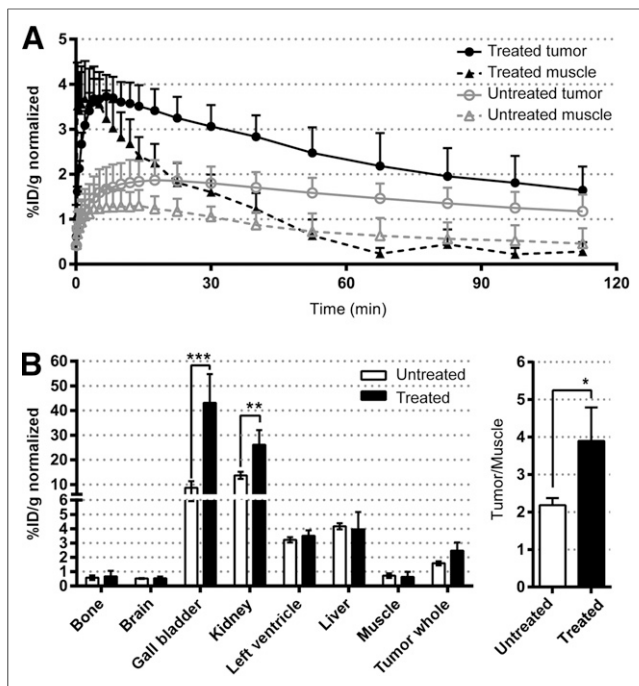


FIGURE 3. Uptake and biodistribution of ^{18}F -C-SNAT in untreated ($n = 6$) and treated ($n = 5$) mice. (A) Time-activity curves derived from tumor and muscle. (B) Image-derived biodistribution in various regions of mice at 60 min after injection. (C) Tumor-to-muscle ratios in both treated and control mice at 60 min after injection.

were all of pharmaceutical grade from commercial vendors. ^{18}F -C-SNAT precursor (Supplemental Fig. 1; supplemental materials are available at <http://jnm.snmjournals.org>) was produced in-house as previously described (21). Mice (female *nu/nu*) were purchased from Charles River Laboratories, and all animal experiments were approved by the Stanford Administrative Panel on Laboratory Animal Care in compliance with all federal and state regulations governing the humane care and use of laboratory animals.

Radiochemistry

^{18}F -C-SNAT was synthesized according to our previously reported procedure (21) with a different catalyst (Supplemental Fig. 1) (28). Briefly, ^{18}F -azide was synthesized via a fully automated ^{18}F /tosylate exchange in a TRACERlab FX-FN module (GE Healthcare) and

purified by semipreparative high-performance liquid chromatography. The purified ^{18}F -azide was conjugated to the peptide precursor by a copper-catalyzed azide-alkyne cycloaddition (CuAAC) using $(\text{BimC}_4\text{A})_3$ as an accelerating ligand to improve the reaction yield (Supplemental Fig. 2) (28). After final purification by semipreparative high-performance liquid chromatography, ^{18}F -C-SNAT was formulated in a solution of 1:10 ethanol/saline (0.9% NaCl in H_2O). The specific activity for each batch of ^{18}F -C-SNAT was calculated on the basis of ^{19}F -C-SNAT calibration curve under ultraviolet light (254 nm). The calibration curve was generated with 5 different concentrations of ^{19}F -C-SNAT.

Animal Model

Mice were housed with free access to food and water and allowed ample time to acclimatize before the experiments. HeLa cells (1–2 million in 0.2 mL of phosphate-buffered saline per mouse) were injected subcutaneously into the shoulder of 6- to 7-wk-old nude mice under anesthesia (2% isoflurane in oxygen at a flow rate of 2 L/min). The tumor xenografts were allowed to grow to a minimum size of 5×5 mm (usually 10–14 d) before treatment was initiated. Mice with tumors larger than 17.5 mm in 1 direction were euthanized, as was any animal showing apparent signs of distress. Treated mice ($n = 5$) received 3 intravenous injections of doxorubicin (8 mg/kg) in saline suspension on days 0, 4, and 8, followed by PET scanning on day 10. Control mice ($n = 6$) received intravenous saline injections. The weight of the mice and growth of tumors was monitored every other day during the course of treatment.

PET

On the day of the experiment, the mice were transported to the imaging facility at least 1 h before the experiment. Mice were anesthetized 1 at a time using isoflurane inhalation (2% isoflurane in oxygen at a flow rate of 2 L/min), and a catheter was placed in the tail vein of the mouse. A bolus of 100 μL of heparinized saline (100 IU/mL heparin) was injected to maintain patency of the catheter and vein, followed by regular small injections to keep patency and hydrate the mouse during the procedure. Eye lubricant was added to the mouse's eyes. The catheterized mouse was placed in 1 of the beds in a custom-made 4×4 mouse bed (29) that can be inserted into an Inveon microPET/CT scanner (Siemens). The mice were kept warm using an infrared warming pad (Kent Scientific) under isoflurane anesthesia. A 15-min CT scan was obtained, followed by intravenous bolus injection of ^{18}F -C-SNAT (8.63 ± 1.02 MBq, $n = 11$) and simultaneous 120-min dynamic PET. The mice were euthanized immediately at the end of imaging acquisition.

The PET data were histogrammed into 21 frames, and each frame was reconstructed using 2-dimensional ordered-subset expectation maximization with arc and scatter correction. One frame (15 min from 45 to 60 min) was reconstructed using 3-dimensional ordered-subset expectation maximization with arc and scatter correction (Fig. 2). The PET and CT images were imported into Inveon Research Workspace 4.0 (Siemens) and coregistered using the automatic affine registration. Two-dimensional images were used to calculate uptake over time, whereas 3-dimensional images were used to generate a 3-dimensional maximum-intensity projection.

Image Analysis

Tracer activity over time was measured for regions of interest in the PET image (mean activity/ cm^3 in the region) using the CT image as an anatomic guide. The left

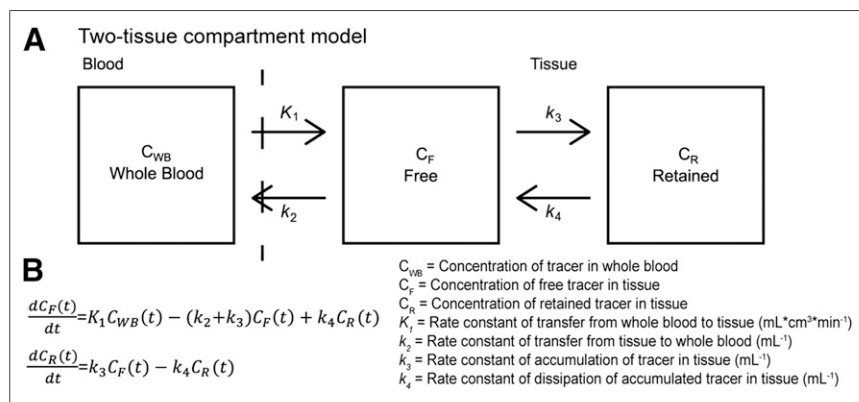


FIGURE 4. Two-tissue compartment model. (A) Compartments and kinetic rate constants. (B) Differential equations describing compartments.

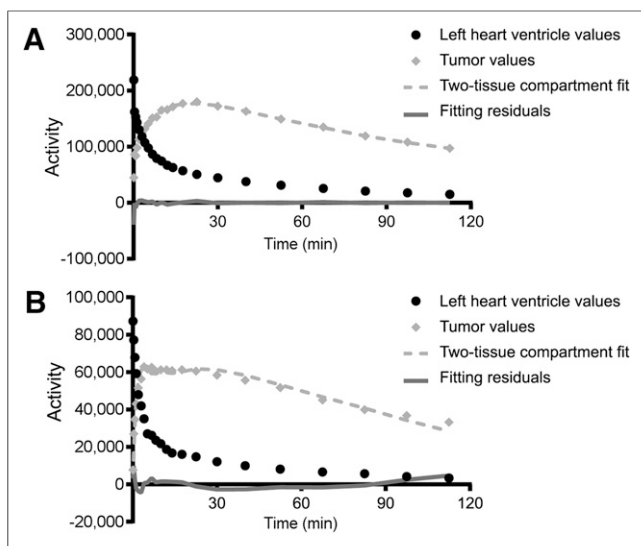


FIGURE 5. Two-tissue-compartment model fitting results, residuals, and original activity data from left heart ventricle and tumor of untreated mouse (A) and treated mouse (B).

ventricle of the heart was hand-drawn on the combined PET/CT image of the first 15 s. The region of the tumor was hand-drawn on the combined PET/CT image at 40 min. The kidney, gallbladder, liver, and brain regions were hand-drawn using the combined PET/CT image at 120 min. The bone and muscle regions were hand-drawn on the left or right upper thigh using the CT image and segregated from each other using a threshold algorithm.

Tumor uptake was calculated as %ID/g and normalized using a normalization factor (NF_x) calculated as the relation between the individual mouse's ventricular activity (area under the curve [AUC] in the left heart ventricle of mouse X over the first 40 min = AUC_x) to the average activity in the left heart ventricle of all mice (AUC_{mean}) ($ID \times NF_x = ID \times AUC_x/AUC_{mean}$) (Supplemental Fig. 3). The summed images from 45 to 60 min were used to generate a complete image-derived biodistribution and tumor-to-muscle ratio (Fig. 3).

Compartmental Modeling

Tracer pharmacokinetics and the kinetic constants K_1 , k_2 , k_3 , and k_4 were calculated by fitting a reversible 2-tissue-compartment model (30,31) to the time-activity curves derived from the tumor and muscle regions (Fig. 3A). The time-activity curve from the left heart ventricle was used as an image-derived input function (further details and evaluation of the image-derived input function are in the supplemental data). The calculations were done using Inveon Research Workspace 4.0.

Statistics

All values are given as value \pm SE of the mean, for the untreated group ($n = 6$) and for the treated group ($n = 5$). Significant differences are calculated using an unpaired 1-sided t test unless otherwise noted, P values less than 0.05 are considered statistically significant, and significance levels in graphs are marked as follows: * $P < 0.05$, ** $P < 0.01$, and *** $P < 0.005$.

RESULTS

Radiochemistry

We have improved the radiochemistry of the synthesis of ^{18}F -C-SNAT using $(\text{BimC}_4\text{A})_3$ as the ligand for the copper-catalyzed azide-alkyne cycloaddition (CuAAC) reaction. There was a positive correlation between the amount of $(\text{BimC}_4\text{A})_3$ and the

reaction yield: 2 equivalents of $(\text{BimC}_4\text{A})_3$ with a reaction time of 5 min resulted in a maximum yield of 80% (Supplemental Fig. 2A). In addition to a higher yield and faster reaction kinetics, the reaction produced less side products, which greatly facilitated the high-performance liquid chromatography purification of the final labeled ^{18}F -C-SNAT (Supplemental Fig. 2B).

^{18}F -C-SNAT was obtained within 3 h using the new radiosynthesis procedure, with an overall radiochemical yield of $14.4\% \pm 0.4\%$ and specific radioactivity of 101.8 ± 31.7 MBq/nmol (decay-corrected to the end of bombardment, based on the ultraviolet light [254 nm] absorbance of ^{19}F -C-SNAT standard calibration curve). Radiochemical purity was greater than 99%, and chemical purity was greater than 95%. The final product was formulated in a 1:10 ethanol/saline (0.9% NaCl in H_2O) mixture with an activity concentration of 86.7 ± 25.2 MBq/mL.

PET

The PET/CT scans were obtained for all 11 mice. Two representative PET images of mice with xenografted HeLa tumors receiving ^{18}F -C-SNAT are shown in Figure 2. The time-resolved uptake (time-activity curve) of ^{18}F -C-SNAT in the tumor and muscle is presented in Figure 3A and corresponding uptake in the liver, kidney, and gallbladder in Supplemental Figure 4. The image-derived biodistribution also includes brain, bone, and bladder at 60 min after injection (Fig. 3B).

We observed an initial 2- to 3-fold increase in the ^{18}F activity in the muscle and liver regions within the first 4 min after injection, combined with an overall faster clearance in treated mice than untreated mice (Fig. 3A; Supplemental Fig. 4). The dominant excretion route was renal clearance, with increased kidney, gallbladder, and bladder uptake over time with a smaller portion of gastrointestinal excretion. The treated tumors had an initial uptake (at 4 min after injection) of 3.7 ± 0.4 %ID/g whereas the untreated tumors had only 1.5 ± 0.2 %ID/g, and 2.5 ± 0.6 %ID/g in treated versus 1.6 ± 0.1 %ID/g in untreated tumors at 60 min after injection (Fig. 3A). The uptake in treated tumors was higher than that in untreated tumors throughout the whole scan.

Using the left or right thigh muscles as a reference region, we calculated the ratio of tumor-to-muscle activity at 60 min after injection of ^{18}F -C-SNAT (Fig. 3C). There was a significantly higher tumor-to-muscle ratio of 3.9 ± 0.9 (2.5 ± 0.6 %ID/g in tumor/ 0.6 ± 0.4 %ID/g in muscle, $P = 0.025$) in treated mice than in untreated mice (2.2 ± 1.9 ; 1.6 ± 0.2 %ID/g in tumor/ 0.7 ± 0.1 %ID/g in muscle).

Pharmacokinetic Analysis

The pharmacokinetics of ^{18}F -C-SNAT in tumor and muscular tissue were successfully modeled using the reversible 2-tissue-compartment model (30,31) with an image-derived input function (Figs. 4 and 5). The model describes the flow of tracer from the blood to the tissue (K_1) and in reverse (k_2) from the tissue into the blood, as well as tracer accumulation in tissue (k_3) and dissipation of the accumulated tracer (k_4) (Fig. 6B; Table 1). The ratio of K_1 over k_2 indicates the net delivery of tracer in the tissue, whereas the ratio of k_3 over k_4 indicates whether the tracer is preferentially retained in the tissue (Fig. 6B; Table 1). The delivery of ^{18}F -C-SNAT from blood into tumor tissue (K_1 tumor) was significantly (3.2 times) higher in response to treatment; a simultaneous increase was found in muscular tissue, with flow rates (K_1 muscle) after treatment similar to those in

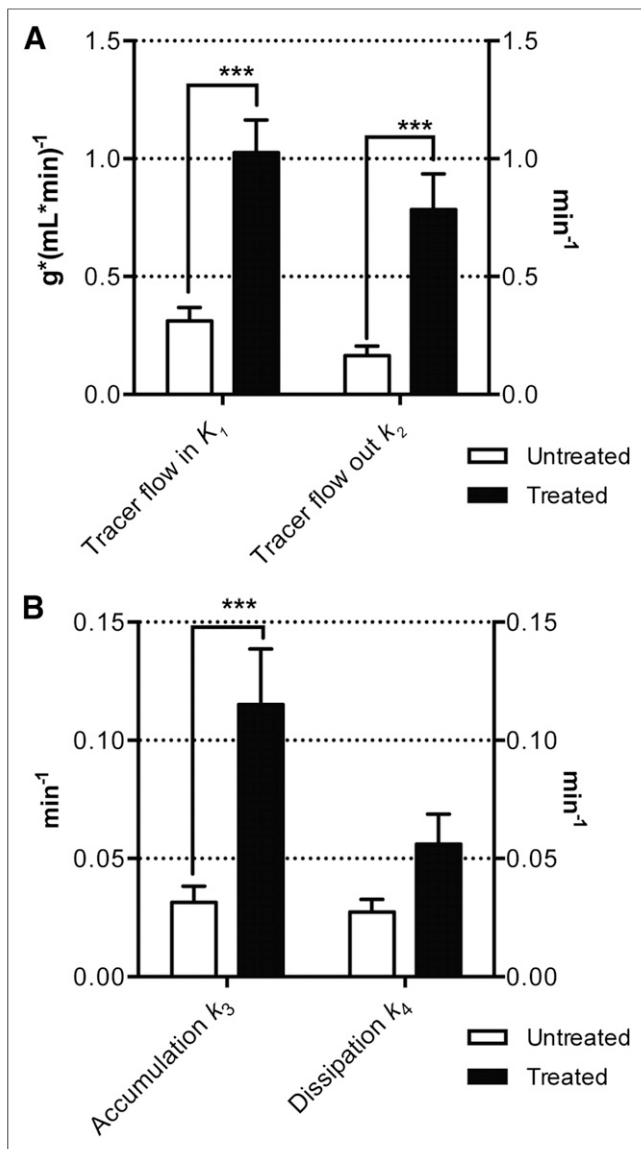


FIGURE 6. Pharmacokinetics of ^{18}F -C-SNAT in untreated ($n = 6$) and treated ($n = 5$) mice. (A) Tracer flow in ($K_1/g \times [mL \times min]^{-1}$) and out (k_2/min^{-1}) of tumor tissue. (B) Accumulation (k_3/min^{-1}) and dissipation (k_4/min^{-1}) of tracer in tumor tissue. ***Statistical significance ($P < 0.005$).

the tumor (Table 1). We also observed an increased flow back into the blood from the tumor tissue (k_2 tumor) and back into the blood from muscle tissue (k_2 muscle). As a result of increases in both K_1 and k_2 , the net delivery of ^{18}F -C-SNAT (K_1/k_2 tumor) to the treated tumor was actually lower than to the untreated tumor (Table 1). Accumulation of ^{18}F -C-SNAT (k_3 tumor) was significantly increased (3.7 times) in treated tumors, and a smaller increase (not significant) in dissipation (k_4 tumor) was also observed, leading to an increase of 1.9 times in the retained amount of ^{18}F -C-SNAT in the treated tumor (expressed as k_3/k_4 tumor), compared with the untreated tumor. The estimated accumulation (k_3 muscle) and dissipation (k_4 muscle) rates of ^{18}F -C-SNAT in muscular tissue were approaching zero (<0.01), suggesting that ^{18}F -C-SNAT was not retained in the region.

DISCUSSION

The current gold standard in measuring treatment response with PET is ^{18}F -FDG metabolism. However, ^{18}F -FDG measurements have been shown to be potentially biased by changes in blood flow after antitumor treatment (25–27) and increased uptake in inflammatory tissue (8,32) and in hypoxic areas of tumors (27,33), leading to false-negatives. Tracer pharmacokinetic modeling has been developed to correct these biases, for example, the delivery rate K_1 or influx K_1 ($K_1 = [K_1 \times k_3]/[k_2 + k_3]$) of ^{18}F -FDG has been shown to correlate better with tumor response to treatment than the standardized uptake value measurement commonly calculated from static PET images (27,34,35). And the kinetics of the SPECT tracer ^{99m}Tc -duramycin were used to examine heart ischemia. However, none of the previous reports on apoptosis PET tracers has undertaken a complete pharmacokinetic analysis to account for increased delivery after systemic chemotherapeutic treatment.

In this study, we applied a full pharmacokinetic evaluation of ^{18}F -C-SNAT to quantify the tracer in vivo kinetics after the clinically relevant systemic chemotherapeutic treatment with doxorubicin. Our pharmacokinetic analysis has shown that the delivery of ^{18}F -C-SNAT (K_1), which is dependent on the blood flow, increased in all regions after chemotherapeutic treatment; this result is similar to what has been reported with ^{18}F -FDG (25–27) and suggests an ancillary response to treatment. A future direct analysis of blood flow changes using ^{15}O -H $_2$ O PET or laser Doppler flowmetry may help to explain this observation and further validate this result. The pharmacokinetic analysis has also shown increased accumulation (k_3) of ^{18}F -C-SNAT in treated tumors, independent of the increased blood flow. In addition, our analysis gave a small dissipation (k_4) rate of the tracer in the tumor tissue, which may be attributed, in part, to the degradation of apoptotic cells and following release of accumulated tracer and to an additional step in the probe mechanism that may not be represented by the 2-tissue-compartment model. Increased delivery (K_1) and small dissipation rate (k_4) contribute to an increased rate of tracer going back into the blood (k_2).

Our analysis of the muscular tissue indicates little tracer accumulation and dissipation (k_3 and k_4 in muscle approach zero), suggesting that muscular tissue could be an acceptable reference region and that tumor-to-muscle ratios might be a valid mean of measurement in systemically treated animals, but more experiments will help further validate this postulation.

In our previous proof-of-principle intratumoral treatment model, we observed around 1 %ID/g in treated tumor and a tumor-to-muscle ratio of 6 after treatment (15). In this study, the mice received a systemic administration of the drug doxorubicin, and there was an increase of approximately 2–3 %ID/g in tumor and a tumor-to-muscle ratio of 3.9. As our pharmacokinetics analysis indicated, the higher tumor signal may be due to a systemic increase in blood flow, and thus tracer delivery, after systemic chemotherapeutic treatment. Other PET studies of tumor response to treatment often fail to take into consideration the blood flow change. The lower tumor-to-muscle ratio was expected because the systemic treatment is believed to be less effective than intratumoral treatments; however, one should be cautious to conclude anything from the tumor-to-muscle ratio because muscular tissue has not been thoroughly tested as a valid reference region in the response to treatment paradigm. It is highly possible that

TABLE 1
Average Pharmacokinetic Rate Constants Calculated for Tumor and Muscle Regions

Rate constant	Untreated		Treated	
	Tumor whole	Muscle	Tumor whole	Muscle
K_1 (g·[mL·min] ⁻¹)	0.31 ± 0.05	0.17 ± 0.03	1.03 ± 0.14*	1.03 ± 0.17*
k_2 (min ⁻¹)	0.16 ± 0.04	0.20 ± 0.10	0.78 ± 0.15*	0.49 ± 0.10
k_3 (min ⁻¹)	0.03 ± 0.01	<0.01	0.12 ± 0.02*	<0.01
k_4 (min ⁻¹)	0.03 ± 0.01	<0.01	0.06 ± 0.01	<0.01
K_1/k_2 (g·mL ⁻¹)	2.08 ± 0.20	1.43 ± 0.27	1.39 ± 0.18*	2.32 ± 0.52
k_3/k_4	1.12 ± 0.15	—	2.13 ± 0.24*	—

*Level of significance in change in treated mice, compared with same region in untreated mice.
 K_1 = tracer flow-in; k_2 = tracer flow-out; k_3 = accumulation; k_4 = dissipation.

systemic effects of treatment could affect the tracer dynamics in the tumor and muscular tissue differently. In comparison with static and ratiometric measurements, preclinical pharmacokinetic analysis of ¹⁸F-C-SNAT delivers a higher sensitivity and significance in the treatment response measurement. Thus, measuring the accumulation rate (k_3) may give a better outcome estimate, which is free from blood flow bias, than the total signal (%ID/g) or the tumor-to-muscle ratio.

Because of the small size of mice as experimental animals in this study, ex vivo input functions through blood sampling is technically challenging (the amount of unmetabolized tracer at a given time point in plasma). Therefore, an image-derived input function was used after a thorough evaluation against a population-based ex vivo metabolite-corrected input function (details on the image-derived input function are in the supplemental data). Although the 2-tissue-compartment model effectively extracted the bias created by the blood flow changes after treatment without overcomplicating the interpretations of the model outcomes, it might be relatively simplified and not fully represent the dynamics of ¹⁸F-C-SNAT. The model can be further refined with adding more compartments to account for the 2 sequential activation events of ¹⁸F-C-SNAT—the cyclization and aggregation. A full pharmacokinetic study with this refined model in a larger species in the future may further help translate this new PET tracer to the clinic.

CONCLUSION

The results of this study have further demonstrated that ¹⁸F-C-SNAT is a promising new apoptosis-specific PET tracer for imaging tumor response to chemotherapy. ¹⁸F-C-SNAT has a significantly increased tumor signal and a significantly increased tumor-to-muscle ratio in a preclinical mouse model of tumor therapy. Furthermore, we showed that ¹⁸F-C-SNAT has a significantly increased accumulation rate (k_3) independent from the systemic increase in delivery (K_1) caused by the chemotherapeutic treatment. Future studies will extend the use of our tracer to other tumor response models and imaging modalities.

DISCLOSURE

The costs of publication of this article were defrayed in part by the payment of page charges. Therefore, and solely to indicate this fact,

this article is hereby marked “advertisement” in accordance with 18 USC section 1734. Financial support for this study was provided by the Stanford University National Cancer Institute (NCI) Centers of Cancer Nanotechnology Excellence (U54CA119367), Stanford ICMIC grant (1P50CA114747-06), Stanford University Department of Radiology internal funds, Stanford Small Animal Imaging Facility, and postdoctoral fellowship support from the Danish Cancer Foundation. No other potential conflict of interest relevant to this article was reported.

REFERENCES

- Fedele C, Tothill RW, McArthur GA. Navigating the challenge of tumor heterogeneity in cancer therapy. *Cancer Discov*. 2014;4:146–148.
- Kalia M. Personalized oncology: recent advances and future challenges. *Metabolism*. 2013;62(suppl 1):S11–S14.
- Eisenhauer EA, Therasse P, Bogaerts J, et al. New response evaluation criteria in solid tumours: revised RECIST guideline (version 1.1). *Eur J Cancer*. 2009;45:228–247.
- Flores LG, Yeh HH, Soghomonyan S, et al. Monitoring therapy with MEK inhibitor U0126 in a novel Wilms tumor model in Wt1 knockout Igf2 transgenic mice using ¹⁸F-FDG PET with dual-contrast enhanced CT and MRI: early metabolic response without inhibition of tumor growth. *Mol Imaging Biol*. 2013;15:175–185.
- Sharma P, Singh H, Basu S, Kumar R. Positron emission tomography-computed tomography in the management of lung cancer: an update. *South Asian J Cancer*. 2013;2:171–178.
- Wahl RL, Jacene H, Kasamon Y, Lodge MA. From RECIST to PERCIST: evolving considerations for PET response criteria in solid tumors. *J Nucl Med*. 2009;50(suppl 1):122S–150S.
- Forner A, Ayuso C, Varela M, et al. Evaluation of tumor response after locoregional therapies in hepatocellular carcinoma: are response evaluation criteria in solid tumors reliable? *Cancer*. 2009;115:616–623.
- Abdulla S, Salavati A, Saboury B, Basu S, Torigian DA, Alavi A. Quantitative assessment of global lung inflammation following radiation therapy using FDG PET/CT: a pilot study. *Eur J Nucl Med Mol Imaging*. 2014;41:350–356.
- Burgman P, Odonoghue JA, Humm JL, Ling CC. Hypoxia-induced increase in FDG uptake in MCF7 cells. *J Nucl Med*. 2001;42:170–175.
- Kim SJ, Lee JS, Im KC, et al. Kinetic modeling of 3'-deoxy-3'-¹⁸F-fluorothymidine for quantitative cell proliferation imaging in subcutaneous tumor models in mice. *J Nucl Med*. 2008;49:2057–2066.
- Smith TA, Zanda M, Fleming IN. Hypoxia stimulates ¹⁸F-fluorodeoxyglucose uptake in breast cancer cells via hypoxia inducible factor-1 and AMP-activated protein kinase. *Nucl Med Biol*. 2013;40:858–864.
- Khan KH, Blanco-Codecido M, Molife LR. Cancer therapeutics: targeting the apoptotic pathway. *Crit Rev Oncol Hematol*. 2014;90:200–219.
- Favaloro B, Allocati N, Graziano V, Di Ilio C, De Laurenzi V. Role of apoptosis in disease. *Aging*. 2012;4:330–349.
- Lev N, Melamed E, Offen D. Apoptosis and Parkinson's disease. *Prog Neuro-psychopharmacol Biol Psychiatry*. 2003;27:245–250.

15. Yagle KJ, Eary JF, Tait JF, et al. Evaluation of ^{18}F -annexin V as a PET imaging agent in an animal model of apoptosis. *J Nucl Med.* 2005;46:658–666.
16. Yao S, Hu K, Tang G, et al. Positron emission tomography imaging of cell death with [^{18}F]FPDduramycin. *Apoptosis.* 2014;19:841–850.
17. Nguyen Q-D, Smith G, Glaser M, Perumal M, Arstad E, Aboagye EO. Positron emission tomography imaging of drug-induced tumor apoptosis with a caspase-3/7 specific [^{18}F]-labeled isatin sulfonamide. *Proc Natl Acad Sci USA.* 2009;106:16375–16380.
18. Challapalli A, Kenny LM, Hallett WA, et al. ^{18}F -ICMT-11, a caspase-3-specific PET tracer for apoptosis: biodistribution and radiation dosimetry. *J Nucl Med.* 2013;54:1551–1556.
19. Witney TH, Fortt RR, Aboagye EO. Preclinical assessment of carboplatin treatment efficacy in lung cancer by ^{18}F -ICMT-11-positron emission tomography. *PLoS ONE.* 2014;9:e91694.
20. Su H, Chen G, Gangadharmath U, et al. Evaluation of [^{18}F]-CP18 as a PET imaging tracer for apoptosis. *Mol Imaging Biol.* 2013;15:739–747.
21. Shen B, Jeon J, Palner M, et al. Positron emission tomography imaging of drug-induced tumor apoptosis with a caspase-triggered nanoaggregation probe. *Angew Chem Int Ed Engl.* 2013;52:10511–10514.
22. Ye D, Liang G, Ma ML, Rao J. Controlling intracellular macrocyclization for the imaging of protease activity. *Angew Chem Int Ed Engl.* 2011;50:2275–2279.
23. Ye D, Shuhendler AJ, Cui L, et al. Bioorthogonal cyclization-mediated in situ self-assembly of small-molecule probes for imaging caspase activity in vivo. *Nat Chem.* 2014;6:519–526.
24. Ye D, Shuhendler AJ, Pandit P, et al. Caspase-responsive smart gadolinium-based contrast agent for magnetic resonance imaging of drug-induced apoptosis. *Chem Sci.* 2014;4:3845–3852.
25. Mankoff DA, Dunnwald LK, Galow JR, et al. Changes in blood flow and metabolism in locally advanced breast cancer treated with neoadjuvant chemotherapy. *J Nucl Med.* 2003;44:1806–1814.
26. Tseng J, Dunnwald LK, Schubert EK, et al. ^{18}F -FDG kinetics in locally advanced breast cancer: correlation with tumor blood flow and changes in response to neoadjuvant chemotherapy. *J Nucl Med.* 2004;45:1829–1837.
27. Røe K, Aleksandersen TB, Kristian A, et al. Preclinical dynamic ^{18}F -FDG PET: tumor characterization and radiotherapy response assessment by kinetic compartment analysis. *Acta Oncol.* 2010;49:914–921.
28. Rodionov VO, Presolski SI, Gardinier S, Lim Y, Finn MG. Benzimidazole and related ligands for Cu-catalyzed azide-alkyne cycloaddition. *J Am Chem Soc.* 2007;129:12696–12704.
29. Habte F, Ren G, Doyle TC, Liu H, Cheng Z, Paik DS. Impact of a multiple mice holder on quantitation of high-throughput microPET imaging with and without CT attenuation correction. *Mol Imaging Biol.* 2013;15:569–575.
30. Innis RB, Cunningham VJ, Delforge J, et al. Consensus nomenclature for in vivo imaging of reversibly binding radioligands. *J Cereb Blood Flow Metab.* 2007;27:1533–1539.
31. Gunn RN, Sargent PA, Bench CJ, et al. Tracer kinetic modeling of the 5-HT_{1A} receptor ligand [carbonyl- ^{11}C]WAY-100635 for PET. *Neuroimage.* 1998;8:426–440.
32. Hicks RJ, Mac Manus MP, Matthews JP, et al. Early FDG-PET imaging after radical radiotherapy for non-small-cell lung cancer: inflammatory changes in normal tissues correlate with tumor response and do not confound therapeutic response evaluation. *Int J Radiat Oncol Biol Phys.* 2004;60:412–418.
33. Pugachev A, Ruan S, Carlin S, et al. Dependence of FDG uptake on tumor microenvironment. *Int J Radiat Oncol Biol Phys.* 2005;62:545–553.
34. Guo J, Guo N, Lang L, et al. ^{18}F -alfatide II and ^{18}F -FDG dual-tracer dynamic PET for parametric, early prediction of tumor response to therapy. *J Nucl Med.* 2014;55:154–160.
35. Dunnwald LK, Doot RK, Specht JM, et al. PET tumor metabolism in locally advanced breast cancer patients undergoing neoadjuvant chemotherapy: value of static versus kinetic measures of fluorodeoxyglucose uptake. *Clin Cancer Res.* 2011;17:2400–2409.